A Single-Layer Dual-Mesh Boundary Element Method for Multiscale Electromagnetic Modeling of Penetrable Objects in Layered Media

Shashwat Sharma, Graduate Student Member, IEEE, and Piero Triverio, Senior Member, IEEE

Abstract—A surface integral representation of Maxwell's equations allows the efficient electromagnetic (EM) modeling of threedimensional structures with a two-dimensional discretization, via the boundary element method (BEM). However, existing BEM formulations either lead to a poorly conditioned system matrix for multiscale problems, or are computationally expensive for objects embedded in layered substrates. This article presents a new BEM formulation which leverages the surface equivalence principle and Buffa-Christiansen basis functions defined on a dual mesh, to obtain a well-conditioned system matrix suitable for multiscale EM modeling. Unlike existing methods involving dual meshes, the proposed formulation avoids the double-layer potential operator for the surrounding medium, which may be a stratified substrate requiring the use of an advanced Green's function. This feature greatly alleviates the computational expense associated with the use of Buffa-Christiansen functions. Numerical examples drawn from several applications, including remote sensing, chip-level EM analysis, and metasurface modeling, demonstrate speed-ups ranging from $3 \times$ to $7 \times$ compared to state-of-the-art formulations.

Index Terms—Maxwell's equations, boundary element method, integral equations, multiscale modeling, layered substrate.

I. INTRODUCTION

THE full-wave electromagnetic simulation of penetrable deliberation objects is crucial in a wide range of applications, spanning multiple scales of frequency, object size, and material properties. For example, metamaterials and metasurfaces are often multiple wavelengths in size, but may contain subwavelength unit cells with intricate geometries. Furthermore, the unit cells may be made of conductive [1] or dielectric [2] materials embedded in a layered substrate. Therefore, for an accurate simulation, the fields must be modeled both inside and outside each unit cell, while taking into account the layered surrounding medium. Other applications include the design and analysis of ground-penetrating radar systems for the detection and reconstruction of objects buried beneath layers of soil and rock [3]–[5]. The objects may be composed of dielectrics, conductors, or both, and may vary greatly in size and material properties. Multiscale penetrable structures are also encountered in electronic packages and integrated circuits,

S. Sharma and P. Triverio are with the Edward S. Rogers Sr. Department of Electrical & Computer Engineering, University of Toronto, Toronto, ON, M5S 3G4 Canada, e-mails: shash.sharma@mail.utoronto.ca, piero.triverio@utoronto.ca.

This work was supported by the Natural Sciences and Engineering Research Council of Canada (Collaborative Research and Development Grants program), by Advanced Micro Devices, and by CMC Microsystems.

Manuscript received ...; revised

where metallic traces and dielectric inclusions may occur in close proximity to each other. Examples include air-backed or suspended on-chip inductor coils [6]–[8].

The boundary element method (BEM), which is based on a surface integral representation of Maxwell's equations [9], has emerged as an important technique for full-wave electromagnetic modeling, since it allows three-dimensional problems to be modeled with a two-dimensional surface mesh [10], [11]. For penetrable objects, the BEM requires solving an internal problem to model fields within objects, and an external problem to model the coupling between them.

Several BEM formulations have been proposed for modeling penetrable objects, but the existing methods have limitations, particularly for multiscale structures embedded in layered media. The Poggio-Miller-Chang-Harrington-Wu-Tsai (PMCHWT) [12]–[14] and related formulations are well-established, but are only accurate when the contrast in electrical properties between adjacent media is not large. This places restrictions on the types of materials which can be modeled.

The generalized impedance boundary condition (GIBC) [15] formulation and related methods [16], [17] can handle a large contrast in material properties, but require the double-layer potential operator [9] for the external problem. When the multilayer Green's function (MGF) [18] is used to model layered surrounding media, the double-layer potential operator requires computing the curl of the MGF in addition to the MGF itself, which significantly increases the computational cost [19] and code complexity. Furthermore, GIBC-based methods involve inner products between Rao-Wilton-Glisson (RWG) basis functions [20] and rotated RWG functions, which leads to a singular identity operator in both the internal and external problems. This operator can deteriorate the convergence of iterative solvers for structures involving both conductive and dielectric objects, as will be shown in Section IV. The enhanced augmented electric field integral equation (eAEFIE) formulation was proposed more recently for dielectrics [21] and lossy conductors [22], and extends the original augmented electric field integral equation (AEFIE) [23], [24], which was applicable only to perfect conductors. Unlike the GIBC, the eAEFIE uses the expensive Buffa-Christiansen (BC) [25] functions, defined on a dual mesh, to obtain excellent convergence of iterative solvers for multiscale structures. However, the eAEFIE also requires the double-layer potential operator in the external problem. Moreover, this double-layer operator involves the BC functions, which compounds the associated computational cost.

The differential surface admittance (DSA) approach [26]-[28] was proposed to avoid the double-layer potential operator in the external problem, but leads to a poorly conditioned system matrix even for relatively simple structures, as shown in [19], [29], in part because it also involves a singular identity operator. Even when combined with BC functions [30], the DSA approach still involves two hypersingular operators which suffer from low-frequency breakdown [31]. A formulation that combines the DSA approach with the Calderón preconditioner [32] was proposed to obtain a wellconditioned matrix [33], which also uses BC functions defined on a dual mesh. However, this formulation includes at least one matrix operator which involves both the MGF and BC functions, which significantly increases the computational cost associated with that matrix. More recently, the single-layer impedance matrix (SLIM) [19] formulation was proposed for lossy conductors. The SLIM formulation, like the DSA, avoids the double-layer operator in the external problem, but is well conditioned without the need for BC functions. This makes the SLIM approach well suited for modeling conductors embedded in layered media, such as high-speed electrical interconnects [34]. However, the SLIM formulation was proposed primarily for modeling conductors, and may lead to a poorly conditioned system matrix for multiscale structures involving both dielectric and conductive objects. Furthermore, some operators involved in the SLIM approach also suffer

In this article, we propose a new formulation for modeling penetrable objects in layered media, which combines the benefits of the eAEFIE and SLIM formulations, while avoiding their drawbacks. The formulation we propose is suitable for modeling both dielectric and conductive objects, and accurately captures the frequency-dependent variations of skin depth in the latter. The proposed technique avoids the double-layer operator in the external problem, making it more computationally efficient than the eAEFIE for objects embedded in layered media. Unlike the SLIM approach, the proposed single-layer formulation also eliminates the lowfrequency breakdown by using the AEFIE in both the internal and external problems. The proposed method employs BC functions defined on a dual mesh to obtain excellent conditioning of the system matrix, even for dielectrics and multiscale structures, unlike the SLIM approach. An important and distinctive feature of the proposed formulation is that integral operators involving the expensive BC functions only appear in the internal problem, which has two advantages:

from low-frequency breakdown.

- All operators which involve BC functions require only the simple homogeneous Green's function, which is available in closed form, rather than the MGF, which is expensive to compute and not expressible in closed form.
- All interactions involving the BC functions are local to each object, which is computationally advantageous particularly when the same object occurs in multiple locations.

Therefore, for layered background media, the proposed formulation leverages the benefits of BC functions but greatly alleviates the associated computational cost, compared to the eAEFIE and the method in [33].

The paper is organized as follows: Section II describes the proposed formulation and provides a detailed comparison to existing techniques. Section III summarizes how acceleration algorithms are incorporated into the proposed method to handle large problems efficiently. In Section IV, we demonstrate the efficiency and good conditioning of the proposed method, compared to existing formulations, for multiscale numerical examples drawn from different applications. Concluding remarks are provided in Section V.

2

II. PROPOSED FORMULATION

We consider the problem of electromagnetic scattering from a penetrable object occupying volume \mathcal{V} , bounded by a surface \mathcal{S} with outward unit normal vector \hat{n} . The object is assumed to be homogeneous with relative permittivity ε_r , relative permeability μ_r , and conductivity σ . The object may be embedded in free space, or in layer l of a stratified background medium. Objects spanning multiple layers are split at the layer interface, and handled as described in [35]. The background medium is denoted by \mathcal{V}_0 . In the case of a layered medium, the l^{th} layer has relative permittivity $\varepsilon_{l,r}$, relative permeability $\mu_{l,r}$, and conductivity σ_l . The time-harmonic fields $[\vec{E}_{\text{inc}} \ (\vec{r}), \vec{H}_{\text{inc}} \ (\vec{r})]$, $\vec{r} \in \mathcal{V}_0$, with cyclical frequency ω , are incident on \mathcal{S} . This leads to the field distributions $[\vec{E} \ (\vec{r}), \vec{H} \ (\vec{r})], \vec{r} \in \mathcal{V}$.

A. Internal Problem

The internal problem is responsible for modeling field distributions in \mathcal{V} . The tangential electric and magnetic fields on \mathcal{S} can be related via the augmented electric field integral equation (AEFIE) formulation [23], [24]. The original AEFIE in [23] was developed for perfect conductors, and must be modified for penetrable objects to include the tangential electric field on \mathcal{S} [21], as

$$\mu_{r}\,\hat{\boldsymbol{n}}\times\mathcal{L}^{(A)}\left[jk_{0}\,\hat{\boldsymbol{n}}'\times\vec{H}\left(\vec{r}'\right)\right] - \varepsilon_{c,r}^{-1}\,\hat{\boldsymbol{n}}\times\nabla\mathcal{L}^{(\phi)}\left[c_{0}\,\rho\left(\vec{r}'\right)\right] - \hat{\boldsymbol{n}}\times\mathcal{K}\left[\eta_{0}^{-1}\,\hat{\boldsymbol{n}}'\times\vec{E}\left(\vec{r}'\right)\right] - \frac{1}{2}\left(\eta_{0}^{-1}\,\hat{\boldsymbol{n}}\times\vec{E}\left(\vec{r}'\right)\right) = 0, \quad \text{(1a)}$$

$$\nabla\cdot\left(jk_{0}\,\hat{\boldsymbol{n}}\times\vec{H}\left(\vec{r}'\right)\right) - k_{0}^{2}\left(c_{0}\,\rho\left(\vec{r}'\right)\right) = 0, \quad \text{(1b)}$$

where $\vec{r}, \vec{r}' \in \mathcal{S}$, and c_0 , k_0 and η_0 are the speed of light, wave number and wave impedance in free space. Primed coordinates represent source points, while unprimed coordinates represent observation points. The relative complex permittivity $\varepsilon_{c,r}$ is defined as

$$\varepsilon_{c,r} = \varepsilon_r - j \frac{\sigma}{\omega \varepsilon_0}.$$
 (2)

Equation (1a) is the conventional electric field integral equation (EFIE) [36], but with charge density $\rho\left(\vec{r}\right)$ taken as a separate unknown [24], while (1b) is the continuity equation relating $\rho\left(\vec{r}\right)$ to $\hat{n}\times\vec{H}\left(\vec{r}\right)$. The integral operators in (1a) are defined as [10]

$$\mathcal{L}^{(A)}\left[\vec{X}\left(\vec{r}'\right)\right] = \int_{\mathcal{S}} d\mathcal{S}' \, \vec{X}\left(\vec{r}'\right) \, G\left(k, \vec{r}, \vec{r}'\right),\tag{3}$$

$$\mathcal{L}^{(\phi)}\left[a\left(\vec{r}'\right)\right] = \int_{\mathcal{S}} d\mathcal{S}' \, a\left(\vec{r}'\right) \, G\left(k, \vec{r}, \vec{r}'\right),\tag{4}$$

$$\mathcal{K}\left[\vec{X}\left(\vec{r}'\right)\right] = \int_{\mathcal{S}} d\mathcal{S}' \,\nabla G\left(k, \vec{r}, \vec{r}'\right) \times \vec{X}\left(\vec{r}'\right), \quad (5)$$

where $k = \sqrt{\varepsilon_{c,r}\mu_r} k_0$ is the wave number associated with the object's material. The homogeneous Green's function is

$$G\left(\vec{r}, \vec{r}'\right) = \frac{e^{-jkr}}{4\pi r},\tag{6}$$

where $r = |\vec{r} - \vec{r}'|$.

A triangular mesh is generated for the surface of the object. In (1), $\hat{n} \times \vec{H}(\vec{r})$ is expanded with divergence-conforming area-normalized RWG functions [20], while $\hat{n} \times \vec{E}(\vec{r})$ is expanded with Buffa Christiansen (BC) functions [25] defined on a barycentric refinement of the original mesh. Quantity $\rho(\vec{r})$ is expanded with area-normalized pulse functions. Equation (1a) is tested with $\hat{n} \times \text{RWG}$ functions, while (1b) is tested with pulse functions. The gradient operator in (1a) is transferred to the testing function [11], and the discretized AEFIE is

$$\begin{bmatrix} \mu_r \mathbf{L}^{(A)} & -\varepsilon_{c,r}^{-1} \mathbf{D}^T \mathbf{L}^{(\phi)} \mathbf{B} \\ \mathbf{F} \mathbf{D} & -k_0^2 \mathbf{I} \end{bmatrix} \begin{bmatrix} jk_0 \mathbf{H} \\ c_0 \boldsymbol{\rho} \end{bmatrix}$$
$$= \begin{bmatrix} (\mathbf{K} + \frac{1}{2} \mathbf{I}_{\times}) & \mathbf{0} \\ \mathbf{0} & \mathbf{I} \end{bmatrix} \begin{bmatrix} \eta_0^{-1} \mathbf{E} \\ \mathbf{0} \end{bmatrix}, \quad (7)$$

where $\mathbf{L}^{(A)}$, $\mathbf{L}^{(\phi)}$ and \mathbf{K} are the discretized $\mathcal{L}^{(A)}$, $\mathcal{L}^{(\phi)}$ and \mathcal{K} operators, respectively. Matrix \mathbf{D} is an incidence matrix, while \mathbf{F} and \mathbf{B} are used to enforce charge neutrality [24]. Definitions of \mathbf{D} , \mathbf{F} and \mathbf{B} can be found in [24]. Matrix \mathbf{I} is the identity, while \mathbf{I}_{\times} is the well-conditioned Gram matrix obtained by testing BC basis functions with $\hat{n} \times \mathbf{RWG}$ functions [32]. Column vectors \mathbf{H} , $\boldsymbol{\rho}$ and \mathbf{E} contain the coefficients of the basis functions associated with $\hat{n} \times \vec{H}(\vec{r})$, $\boldsymbol{\rho}(\vec{r})$, and $\hat{n} \times \vec{E}(\vec{r})$, respectively. For highly conductive objects, specialized integration routines [15] are used to compute the entries of $\mathbf{L}^{(A)}$, $\mathbf{L}^{(\phi)}$ and \mathbf{K} , to capture the fast oscillations of the Green's function.

Next, in order to avoid the double-layer operator in the external problem, the surface equivalence principle [37] is invoked to replace the object with the surrounding material, while keeping $\hat{n} \times \vec{E}\left(\vec{r}\right)$ unchanged for $\vec{r} \in \mathcal{S}$ [26]. A pair of equivalent differential sources, $\vec{J}_{\Delta}\left(\vec{r}\right)$ and $\rho_{\Delta}\left(\vec{r}\right)$,

$$\begin{bmatrix} \vec{J}_{\Delta} \left(\vec{r} \right) \\ \rho_{\Delta} \left(\vec{r} \right) \end{bmatrix} = \begin{bmatrix} \hat{n} \times \vec{H} \left(\vec{r} \right) - \hat{n} \times \vec{H}_{eq} \left(\vec{r} \right) \\ \rho \left(\vec{r} \right) - \rho_{eq} \left(\vec{r} \right) \end{bmatrix}, \tag{8}$$

must be introduced on \mathcal{S} to keep fields in \mathcal{V}_0 unchanged. In (8), $\hat{n} \times \vec{H}_{\rm eq} \left(\vec{r} \right)$ and $\rho_{\rm eq} \left(\vec{r} \right)$ are the tangential magnetic field and surface charge density on \mathcal{S} , respectively, in the equivalent configuration. Keeping $\hat{n} \times \vec{E} \left(\vec{r} \right)$ unchanged is the key to avoiding the double-layer potential operator in the external problem [26].

In (8), \vec{J}_{Δ} , $\hat{n} \times \vec{H}(\vec{r})$ and $\hat{n} \times \vec{H}_{eq}(\vec{r})$ are expanded with RWG functions, while $\rho_{\Delta}(\vec{r})$, $\rho(\vec{r})$ and $\rho_{eq}(\vec{r})$ are expanded with pulse functions. This yields

$$\begin{bmatrix} \mathbf{J}_{\Delta} \\ \boldsymbol{\rho}_{\Delta} \end{bmatrix} = \begin{bmatrix} \mathbf{H} - \mathbf{H}_{eq} \\ \boldsymbol{\rho} - \boldsymbol{\rho}_{eq} \end{bmatrix}, \tag{9}$$

where \mathbf{J}_{Δ} and \mathbf{H}_{eq} contain the coefficients of the basis functions associated with \vec{J}_{Δ} and $\hat{n} \times \vec{H}_{\mathrm{eq}}$ (\vec{r}), respectively. Column vectors $\boldsymbol{\rho}_{\Delta}$ and $\boldsymbol{\rho}_{\mathrm{eq}}$ contain the basis function coefficients associated with $\boldsymbol{\rho}_{\Delta}$ (\vec{r}) and $\boldsymbol{\rho}_{\mathrm{eq}}$ (\vec{r}), respectively.

The AEFIE [24] is invoked again in the equivalent configuration to relate $\hat{n} \times \vec{H}_{\rm eq}(\vec{r})$, $\hat{n} \times \vec{E}(\vec{r})$ and $\rho_{\rm eq}(\vec{r})$, which in discrete form is

$$\begin{bmatrix} \mu_{l,r} \mathbf{L}_{l}^{(A)} & -\varepsilon_{l,r}^{-1} \mathbf{D}^{T} \mathbf{L}_{l}^{(\phi)} \mathbf{B} \\ \mathbf{F} \mathbf{D} & -k_{0}^{2} \mathbf{I} \end{bmatrix} \begin{bmatrix} jk_{0} \mathbf{H}_{eq} \\ c_{0} \boldsymbol{\rho}_{eq} \end{bmatrix}$$
$$= \begin{bmatrix} (\mathbf{K}_{l} + \frac{1}{2} \mathbf{I}_{\times}) & \mathbf{0} \\ \mathbf{0} & \mathbf{I} \end{bmatrix} \begin{bmatrix} \eta_{0}^{-1} \mathbf{E} \\ \mathbf{0} \end{bmatrix}. \quad (10)$$

Equation (10) is analogous to (7), except that it corresponds to the equivalent configuration where the objects have been replaced by the surrounding medium [26]. To obtain (10), $\hat{n} \times \vec{E}(\vec{r})$ was expanded with BC functions, and the AEFIE was tested with $\hat{n} \times \text{RWG}$ and pulse functions, as in the original configuration. In (10), $\mathbf{L}_l^{(A)}$, $\mathbf{L}_l^{(\phi)}$ and \mathbf{K}_l are the discretized $\mathcal{L}^{(A)}$, $\mathcal{L}^{(\phi)}$, and \mathcal{K} operators, respectively, involving the homogeneous Green's function associated to layer l of the background medium. In order to eliminate $\mathbf{H}_{\rm eq}$ and $\boldsymbol{\rho}_{\rm eq}$ from the final system of equations, (10) is rearranged as

$$\begin{bmatrix} jk_0\mathbf{H}_{eq} \\ c_0\boldsymbol{\rho}_{eq} \end{bmatrix} = \begin{bmatrix} \mathbf{Y}_{11} & \mathbf{Y}_{12} \\ \mathbf{Y}_{21} & \mathbf{Y}_{22} \end{bmatrix} \begin{bmatrix} \eta_0^{-1} \mathbf{E} \\ \mathbf{0} \end{bmatrix} = \begin{bmatrix} \eta_0^{-1} \mathbf{Y}_{11} \mathbf{E} \\ \eta_0^{-1} \mathbf{Y}_{21} \mathbf{E} \end{bmatrix}, (11)$$

where we have introduced the admittance-like matrix operator,

$$\begin{bmatrix} \mathbf{Y}_{11} & \mathbf{Y}_{12} \\ \mathbf{Y}_{21} & \mathbf{Y}_{22} \end{bmatrix} = \begin{bmatrix} \mu_{l,r} \mathbf{L}_{l}^{(A)} & -\varepsilon_{l,r}^{-1} \mathbf{D}^{T} \mathbf{L}_{l}^{(\phi)} \mathbf{B} \\ \mathbf{F} \mathbf{D} & -k_{0}^{2} \mathbf{I} \end{bmatrix}^{-1} \cdot \begin{bmatrix} (\mathbf{K}_{l} + \frac{1}{2} \mathbf{I}_{\times}) & \mathbf{0} \\ \mathbf{0} & \mathbf{I} \end{bmatrix}. \quad (12)$$

In Section III, we will describe how the matrix inversion in (12) can be handled efficiently without the need for direct factorization, even for large problems. Section IV demonstrates that the proposed method compares favorably to existing techniques such as the eAEFIE [21] for layered medium problems, despite the additional matrix operators required in the equivalent configuration (10).

B. External Problem

Having applied the equivalence theorem, the objects have been replaced by the differential sources $\vec{J}_{\Delta}\left(\vec{r}\right)$ and $\rho_{\Delta}\left(\vec{r}\right)$, which radiate into the surrounding homogeneous or layered medium. These sources are used to model the external problem by relating them to the incident fields via the AEFIE [24]. Expanding $\vec{J}_{\Delta}\left(\vec{r}\right)$, $\hat{n}\times\vec{E}\left(\vec{r}\right)$ and $\rho_{\Delta}\left(\vec{r}\right)$ with RWG, BC and pulse functions, respectively, then testing the AEFIE as before,

$$\begin{bmatrix} \mathbf{L}_{m}^{(A)} & -\mathbf{D}^{T} \mathbf{L}_{m}^{(\phi)} \mathbf{B} \\ \mathbf{F} \mathbf{D} & -k_{0}^{2} \mathbf{I} \end{bmatrix} \begin{bmatrix} jk_{0} \mathbf{J}_{\Delta} \\ c_{0} \boldsymbol{\rho}_{\Delta} \end{bmatrix} + \begin{bmatrix} \mathbf{I}_{\times} & \mathbf{0} \\ \mathbf{0} & \mathbf{I} \end{bmatrix} \begin{bmatrix} \eta_{0}^{-1} \mathbf{E} \\ \mathbf{0} \end{bmatrix} = \begin{bmatrix} \eta_{0}^{-1} \mathbf{E}_{\text{inc}} \\ \mathbf{0} \end{bmatrix}, \quad (13)$$

where subscript m indicates the use of the dyadic multilayer Green's function (MGF) of the background medium as the kernel of the associated integral operator [18]. We now seek

a final system of equations in terms of the unknowns \mathbf{H} , \mathbf{E} and $\boldsymbol{\rho}$. Using (9) in (13) and rearranging, we obtain

$$\begin{bmatrix} \mathbf{L}_{m}^{(A)} & -\mathbf{D}^{T} \mathbf{L}_{m}^{(\phi)} \mathbf{B} \\ \mathbf{F} \mathbf{D} & -k_{0}^{2} \mathbf{I} \end{bmatrix} \begin{bmatrix} jk_{0} \mathbf{H} \\ c_{0} \boldsymbol{\rho} \end{bmatrix}$$

$$- \begin{bmatrix} \mathbf{L}_{m}^{(A)} & -\mathbf{D}^{T} \mathbf{L}_{m}^{(\phi)} \mathbf{B} \\ \mathbf{F} \mathbf{D} & -k_{0}^{2} \mathbf{I} \end{bmatrix} \begin{bmatrix} jk_{0} \mathbf{H}_{eq} \\ c_{0} \boldsymbol{\rho}_{eq} \end{bmatrix}$$

$$+ \begin{bmatrix} \mathbf{I}_{\times} & \mathbf{0} \\ \mathbf{0} & \mathbf{I} \end{bmatrix} \begin{bmatrix} \eta_{0}^{-1} \mathbf{E} \\ \mathbf{0} \end{bmatrix} = \begin{bmatrix} \eta_{0}^{-1} \mathbf{E}_{inc} \\ \mathbf{0} \end{bmatrix}. \quad (14)$$

Next, using (11) in (13) and rearranging terms gives

$$\begin{bmatrix} \mathbf{L}_{m}^{(A)} & \mathbf{C}_{1} & -\mathbf{D}^{T} \mathbf{L}_{m}^{(\phi)} \mathbf{B} \\ \mathbf{F} \mathbf{D} & \mathbf{C}_{2} & -k_{0}^{2} \mathbf{I} \end{bmatrix} \begin{bmatrix} j k_{0} \mathbf{H} \\ \eta_{0}^{-1} \mathbf{E} \\ c_{0} \boldsymbol{\rho} \end{bmatrix} = \begin{bmatrix} \eta_{0}^{-1} \mathbf{E}_{\text{inc}} \\ \mathbf{0} \end{bmatrix}, \quad (15)$$

where

$$\mathbf{C}_{1} = \mathbf{I}_{\times} - \left(\mathbf{L}_{m}^{(A)} \mathbf{Y}_{11} - \mathbf{D}^{T} \mathbf{L}_{l}^{(\phi)} \mathbf{B} \mathbf{Y}_{21} \right), \tag{16}$$

$$\mathbf{C}_2 = -\left(\mathbf{FDY}_{11} - k_0^2 \,\mathbf{Y}_{21}\right). \tag{17}$$

Finally, we use the first equation of (7) in (15) to obtain the proposed single-layer dual-mesh formulation,

$$\begin{bmatrix} \mathbf{L}_{m}^{(A)} & \mathbf{C}_{1} & \mathbf{D}^{T} \mathbf{L}_{m}^{(\phi)} \mathbf{B} \\ \mu_{r} \mathbf{L}^{(A)} & \mathbf{K} & \varepsilon_{c,r}^{-1} \mathbf{D}^{T} \mathbf{L}^{(\phi)} \mathbf{B} \\ \mathbf{F} \mathbf{D} & \mathbf{C}_{2} & k_{0}^{2} \mathbf{I} \end{bmatrix} \begin{bmatrix} jk_{0} \mathbf{H} \\ \eta_{0}^{-1} \mathbf{E} \\ -c_{0} \boldsymbol{\rho} \end{bmatrix} = \begin{bmatrix} \underline{\mathbf{E}}_{\text{inc}} \\ \mathbf{0} \\ \mathbf{0} \end{bmatrix}, (18)$$

where

$$\mathbf{K} = \mathbf{K} + \frac{1}{2} \mathbf{I}_{\times}. \tag{19}$$

C. Structures with Multiple Objects

Next, we generalize the proposed formulation (18) to the case of structures containing multiple disjoint objects, which is easily accomplished with a block-diagonal concatenation of the internal problem matrices. Suppose that A represents any of the blocks in the matrices in (7) or (10). For multiple objects, we may write

$$\mathbf{A} = \operatorname{diag} \begin{bmatrix} \mathbf{A}_1 & \mathbf{A}_2 & \cdots & \mathbf{A}_{N_{\text{obj}}} \end{bmatrix}, \tag{20}$$

where $N_{
m obj}$ is the total number of disjoint objects. The appropriate material properties associated with the $i^{\rm th}$ object must be used in A_i . A key feature of the proposed formulation is that the expensive BC functions are involved only in the matrix operators of (7) and (10), and not in the external problem (13). The only exception is the sparse Gram matrix I_{\times} in (13), which does not involve a Green's function and is very quick to compute. Therefore, thanks to the block-diagonal structure implied by (20), integral operators involving BC functions are local to each object, while the inter-object couplings encoded in $\mathbf{L}_{\mathrm{m}}^{(A)}$ and $\mathbf{L}_{\mathrm{m}}^{(\phi)}$ only involve RWG functions. This is computationally advantageous for multi-object structures, because it implies fewer source-test interactions involving BC functions, compared to the eAEFIE [21] and the method in [33], where BC functions are involved in both intra- and inter-object interactions. As shown in Section IV, CPU time savings up to nearly $7 \times$ are achieved compared to the eAEFIE.

D. Discussion and Comparison to the eAEFIE

The form of (18) resembles that of the eAEFIE [21], except for the blocks which contain C_1 and C_2 . The counterparts to C_1 and C_2 in the eAEFIE are

$$\mathbf{C}_{1}^{[21]} = \mathbf{K}_{\mathrm{m}} - \frac{1}{2} \mathbf{I}_{\times},\tag{21}$$

4

$$\mathbf{C}_{2}^{[21]} = \mathbf{0},$$
 (22)

where \mathbf{K}_{m} is associated to the external problem, and is the discretized double-layer operator \mathcal{K} for the surrounding medium. The key distinction of the proposed formulation is that we use the equivalence principle and the differential sources $\vec{J}_{\Delta}\left(\vec{r}\right)$ and $\rho_{\Delta}\left(\vec{r}\right)$ to avoid \mathbf{K}_{m} . This leads to a significant computational advantage over the eAEFIE in applications involving objects embedded in layered media, for the following reasons:

- 1) The proposed method requires only the single-layer operator in the external problem, which involves computing the MGF [18]. In contrast, due to the presence of K_m, the eAEFIE requires not only the MGF, but also its curl [18]. The curl of the MGF is approximately as expensive to compute as the MGF itself, which can lead to a 2× increase in computational cost compared to a formulation that requires only the MGF [19].
- 2) In the proposed formulation, BC functions only appear in integral operators associated with the *internal* problem, (7) and (10), which involve the simple homogeneous Green's function (6). Therefore, the MGF and the BC functions never occur simultaneously in the same operator. Instead in the eAEFIE, \mathbf{K}_{m} is associated with the external problem, and involves not only the use of BC basis functions, but also the curl of the MGF. Considering point 1) above, the presence of both the curl of the MGF and BC functions in the same operator is especially expensive, since computations involving BC functions can be $6 \times$ more expensive than those involving only RWG functions. This point contributes significantly to the computational advantage of the proposed approach compared to the eAEFIE, as verified in Section IV.
- 3) In the proposed formulation, the computational cost associated with BC functions can be further reduced for structures where the same object occurs in multiple locations. Examples include the use of repeated unit cells in antenna arrays and metasurfaces, and arrays of vias and ground bars often encountered in on-chip passive components and interconnects. In these cases, as long as the mesh is identical for each repeated object, the same internal problem matrices can be reused, leading to significant computational savings. Though this can also be done for the eAEFIE formulation, the reuse of internal problem matrices provides a greater advantage to the proposed formulation. This is because in the eAEFIE, BC functions are used in both the internal and external problems. Therefore, even in the best-case scenario of only one unique object in the structure, only some of the computations related to BC functions

(those associated with the internal problem) can be reused. In the proposed method, BC functions only appear in the internal problem. This allows reusing *all* computations associated with the BC functions, for the objects which are repeated. For simplicity, the internal problem matrices were not reused in any of the examples considered in Section IV.

At the same time, the proposed formulation (18) also retains three key features of the eAEFIE, which contribute to its good conditioning:

- Each block along the diagonal is well conditioned, particularly K, due the use of a dual mesh and BC functions.
- The blocks of (18) are strategically scaled similarly to the eAEFIE, which contributes towards stability at low frequencies.
- When using an iterative solver, the form of (18) allows using a powerful preconditioner similar to the one proposed for the eAEFIE, as described in Section III, which significantly reduces the number of iterations required.

Therefore, the proposed method is able to exploit the features of the eAEFIE which lead to good conditioning, while offering a significant computational advantage for the case of layered surrounding media.

III. ACCELERATION FOR LARGE MULTISCALE PROBLEMS

To handle large structures, we propose an acceleration scheme for the proposed formulation which provides an overall $\sim \mathcal{O}(N^{1.5}\log N)$ time complexity, where N is the total number of unknowns in (18). The adaptive integral method (AIM) [38] is employed in both the external and internal problems, along with an iterative solver. In (18), the matrices $\mathbf{L}_m^{(A)}$ and $\mathbf{L}_m^{(\phi)}$ are compressed via a specialization of the AIM for layered media [35]. Instead, $\mathbf{L}^{(A)}$, $\mathbf{L}^{(\phi)}$, and \mathbf{K} are straightforward to compress via the conventional AIM for both dielectrics and conductors [39], since they involve the homogeneous Green's function (6). In (16) and (17), \mathbf{Y}_{11} and \mathbf{Y}_{21} are not computed explicitly. Instead, the products $\mathbf{Y}_{11}\mathbf{E}^{(i)}$ and $\mathbf{Y}_{21}\mathbf{E}^{(i)}$ are computed on-the-fly at each iteration i during the iterative solution of (18), as follows.

Given $\mathbf{E}^{(i)}$, the system of equations (10) can be solved for $\left[jk_0\mathbf{H}_{\mathrm{eq}}^{(i)}\ c_0\boldsymbol{\rho}_{\mathrm{eq}}^{(i)}\right]^T$ at the i^{th} iteration, which directly yields $\mathbf{Y}_{11}\mathbf{E}^{(i)}$ and $\mathbf{Y}_{21}\mathbf{E}^{(i)}$ via (11). For structures with multiple objects, (10) is solved independently for each object. For objects which are sufficiently small (less than 1000 mesh triangles [39]), we use direct factorization. For larger objects, (10) is also solved with an iterative solver, and the AIM is applied independently for each object [39], to compress the matrices $\mathbf{L}_{l}^{(A)}$, $\mathbf{L}_{l}^{(\phi)}$, and \mathbf{K}_{l} . In these cases, since the iterative solution of (10) is "nested" into the iterative solution of (18), an effective preconditioner is needed to ensure that (10) is solved quickly at each iteration i. To this end, we use the constraint preconditioner proposed in [24]. If each object is relatively small compared to the full structure, the near-region entries of $\mathbf{L}_{l}^{(A)}$ and $\mathbf{L}_{l}^{(\phi)}$ can also be used in the preconditioner [40] to further reduce the iteration count for solving (10). The results in Section IV confirm that the need to solve (10) at each iteration i during the solution of (18) does

not have a significant adverse effect on the overall simulation time

The iterative solution of (18) also requires an effective preconditioner. Due to the similarlity of (18) to the system of equations in the eAEFIE [21], we use a sparse preconditioner similar to the one proposed in [21], defined as

$$\mathbf{P} = \begin{bmatrix} \operatorname{diag} \mathbf{L}_{m}^{(A)} & \operatorname{diag} \mathbf{I}_{\times} & \mathbf{D}^{T} \operatorname{diag} \mathbf{L}_{l}^{(\phi)} \mathbf{B} \\ \mu_{r} \operatorname{diag} \mathbf{L}^{(A)} & \operatorname{diag} \mathbf{K} & \varepsilon_{c,r}^{-1} \mathbf{D}^{T} \operatorname{diag} \mathbf{L}^{(\phi)} \mathbf{B} \\ \mathbf{FD} & \mathbf{0} & k_{0}^{2} \mathbf{I} \end{bmatrix}$$
(23)

As described in [21], the analytical block inverse of \mathbf{P} can be constructed using the Schur complement, so that the preconditioner can be applied on-the-fly during the i^{th} iteration. Consequently, only a small number of iterations is needed even for very challenging problems, and the convergence behaviour of the proposed formulation is nearly identical to that of the eAEFIE, as will be shown in Section IV.

IV. RESULTS

In this section, the accuracy and performance of the proposed formulation are demonstrated through comparisons with state-of-the-art techniques from the literature. All simulations were performed single-threaded on a 3 GHz Intel Xeon CPU with 256 GB of memory. The GMRES iterative solver [41] available in the scientific computation library PETSc [42] was used to solve (10) and (18). A relative residual norm of 10^{-4} was used as the convergence tolerance for GMRES in all cases. The surface current distributions were plotted with scientific colormaps taken from [43].

To expedite the computation of the MGF [18] during the direct integration step, the quasistatic part of the MGF is extracted in the spectral domain, and added back in analytical form in the spatial domain [44]. This speeds up the computation of the Sommerfeld integrals [45] for the terms remaining after the quasistatic extraction. To avoid computing these integrals for every source-test interaction, interpolation tables are precomputed.

A. Dielectric Sphere in Free Space

To validate the accuracy of the proposed formulation, we consider a dielectric sphere in free space, with relative permittivity 12 and diameter 1 m. The sphere is centered at the origin and meshed with 2114 triangles. A plane wave, traveling in the -z direction with the electric field polarized along the xaxis, is incident on the sphere. The radar cross section (RCS) is measured and compared to the analytical solution obtained via the Mie series. Fig. 1 demonstrates excellent agreement in both the monostatic and bistatic RCS between the proposed method and the Mie series. The top panel of Fig. 2 shows the number of GMRES iterations required for convergence over a wide range of frequencies, for the proposed method compared to existing formulations. Both the proposed and the eAEFIE [21] formulations show excellent convergence even at extremely low frequencies, while the GIBC [15] and SLIM [19] formulations fail to converge within 1000 iterations, except above $\sim 10^5$ Hz. The bottom panel of Fig. 2 shows the CPU time per frequency, which in this case is

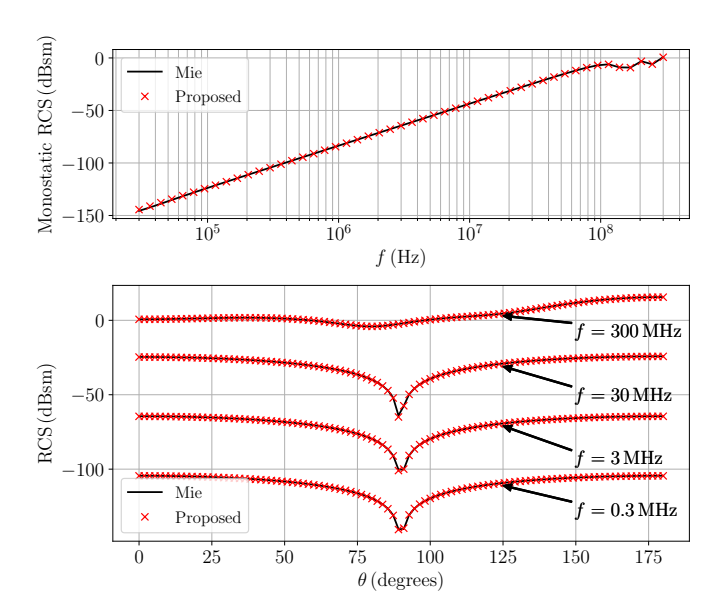


Fig. 1: Accuracy validation for the sphere in Section IV-A. Top: monostatic RCS as a function of frequency. Bottom: bistatic RCS as a function of elevation angle, for $\phi = 0$.

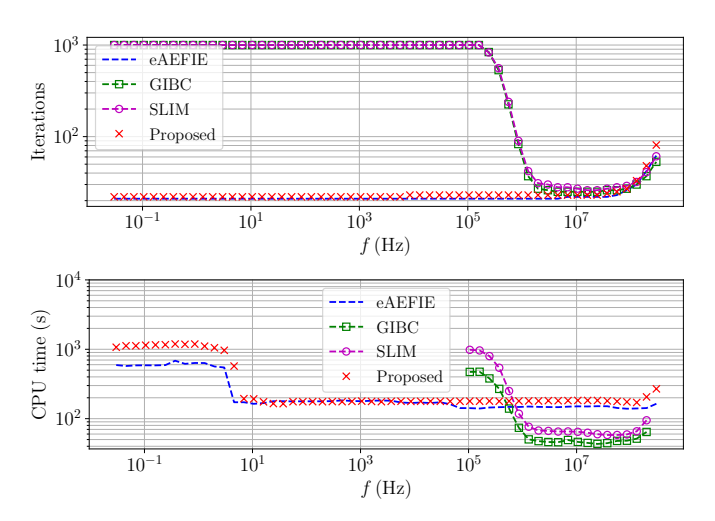


Fig. 2: Performance comparison for the sphere in Section IV-A. Top: GMRES iterations. Bottom: CPU time.

comparable to the CPU time for the eAEFIE, since the surrounding medium is homogeneous. The fact that the GIBC and SLIM formulations avoid the use of BC basis functions is only advantageous over a relatively narrow frequency range, between approximately $10^6\,\mathrm{Hz}$ and $10^8\,\mathrm{Hz}$.

B. Sphere Array Buried Underground

Next, we demonstrate the scalability of the proposed method in the context of a remote sensing application. An array of dielectric spheres, each with relative permittivity 12 and diameter $250\,\mathrm{mm}$, is embedded in the layered medium described in the first column of Table I. The considered dielectric layers represent typical electrical parameters of layered models of the ground [5]. We consider array sizes ranging from 2×2 to 14×14 spheres, and the 4×4 case is visualized in Fig. 3.

TABLE I: Dielectric layer configurations for the numerical examples in Section IV. Layers are non-magnetic, and h denotes the layer's height.

Sphere array (Section IV-B)				Inductor coil (Section IV-C)		SRR array (Section IV-D)	
ε_r	σ (S/m)	h (mm)	$ $ ε_r	h (µm)	ε_r	h (µm)	
	Air	∞	Air	∞	Air	∞	
3.47	0.001725	525	3.7 11.9 4.4	50 30 20	3.7 4.4 2.1	5 4 15	
6.5	0.003338	∞	PEC	∞	PEC	∞	

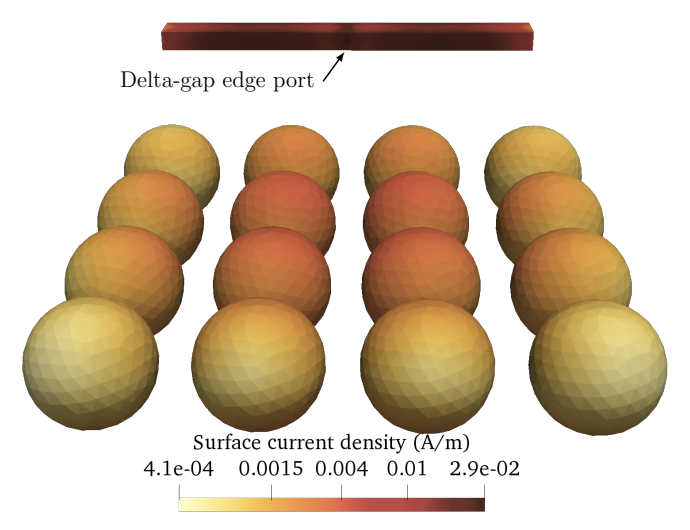


Fig. 3: Geometry and electric surface current density at 200 MHz for the array of spheres in Section IV-B, excited by a dipole antenna.

In each case, the array is centered at the origin, and the bottom of the dielectric layer is located at $z=-150\,\mathrm{mm}$. A dipole antenna, designed to be half a wavelength long at $200\,\mathrm{MHz}$, is used to excite the array. The antenna is modeled as a rectangular prism with dimensions $75\,\mathrm{mm} \times 750\,\mathrm{mm} \times 37.5\,\mathrm{mm}$, and is centered at the point $(0,0,493.75\,\mathrm{mm})$. A delta-gap edge port [11] is defined at the center of the dipole as shown in Fig. 3, where the scattering parameter S_{11} is measured.

Fig. 4 shows the magnitude (top panel) and phase (bottom panel) of S_{11} in the vicinity of the antenna's design frequency, for the cases of 2×2 and 4×4 spheres. Also shown is the case with the antenna alone, in the absence of any spheres. The results are compared against those obtained with the commercial solver Altair Feko. Excellent agreement is observed over the entire bandwidth of the dipole in all cases. The top panel of Fig. 5 shows the GMRES iterations required for convergence as a function of the number of triangles, and demonstrates that the proposed method remains nearly as well conditioned as the eAEFIE, even as the problem size increases. The bottom panel of Fig. 5 shows the total CPU time as a function of the number of triangles. It demonstrates the significant improvement in performance of the proposed method compared to the eAEFIE, ranging from a $6.8\times$ speed-up for the 2×2 array, to a $5.2\times$

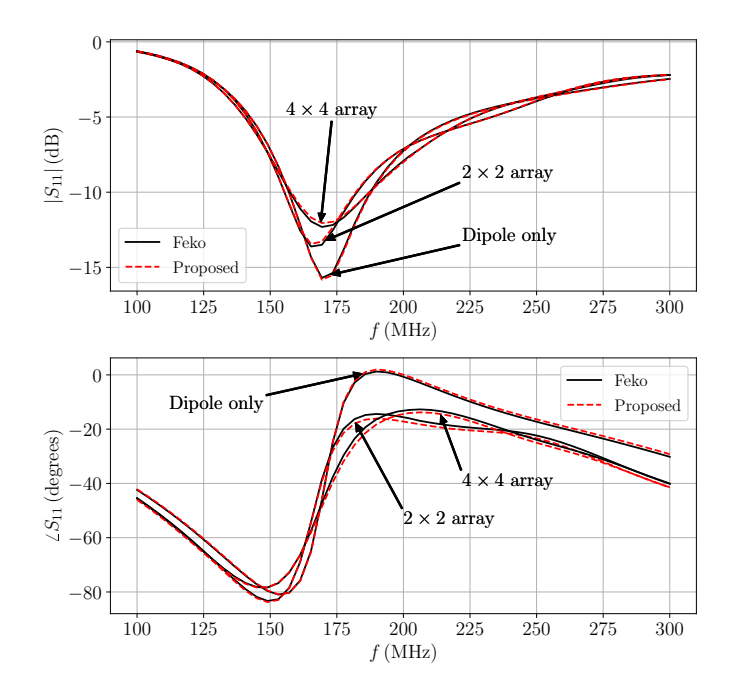


Fig. 4: Scattering parameter validation for the array of spheres in Section IV-B. Top: magnitude. Bottom: phase.

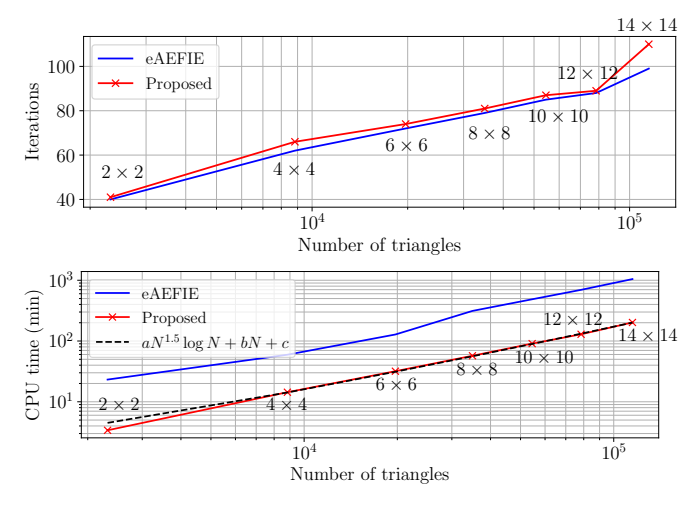


Fig. 5: Performance comparison for the array of spheres in Section IV-B. Top: GMRES iterations. Bottom: CPU time per frequency. Fit parameters are $a=1.92\times 10^{-7}$, $b=1.41\times 10^{-3}$, c=1.16, and N is the number of triangles.

speed-up for the 14×14 array. The fact that the double-layer operator is avoided in the external problem is primarily responsible for the efficiency of the proposed method compared to the eAEFIE. Also shown in Fig. 5 is a curve fit to the CPU time data for the proposed method, which confirms the predicted $\mathcal{O}(N^{1.5}\log N)$ performance, where N is the number of mesh triangles.

C. Inductor Coil with Microvias and a Dielectric Inclusion

Here, we apply the proposed formulation to analyze an onchip inductor coil involving a microvia array, backed by an air pocket, shown in Fig. 6. Air pockets are often introduced

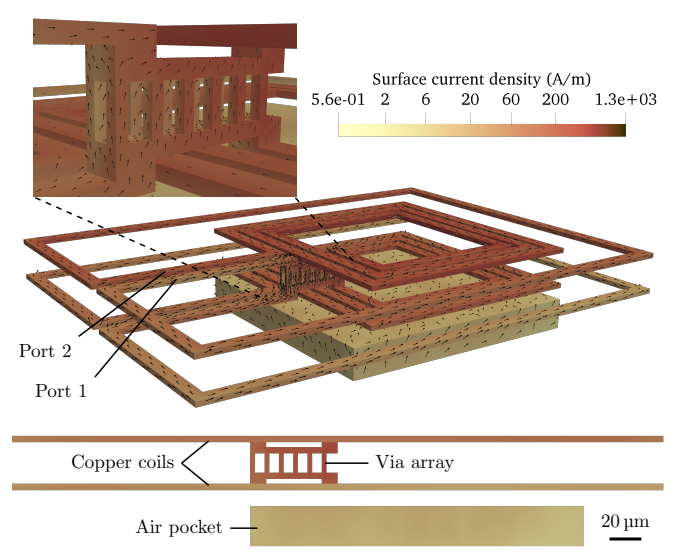


Fig. 6: Geometry and electric surface current density at 10 GHz for the inductor coil in Section IV-C. Inset shows a close-up of the microvia array.

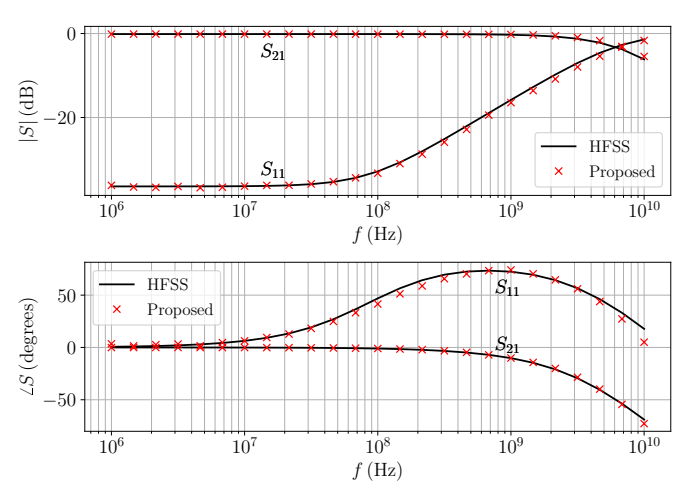


Fig. 7: Scattering parameter validation for the inductor coil in Section IV-C. Top: magnitude. Bottom: phase.

beneath inductor coils to reduce parasitic effects [6]-[8]. Since air pockets are finite in size, they cannot be modeled as part of the background medium with the MGF. Instead, the air pockets must be treated as dielectric objects whose surfaces are also meshed. However, the proximity of a dielectric object to the metallic coils can lead to poor matrix conditioning in existing BEM formulations such as the GIBC [15] and SLIM [19] approaches, as will be shown this section. The presence of a microvia array further adds to the complexity of the problem, because the small features of the vias require a locally dense discretization. Moreover, on-chip passive components must be characterized over a broad frequency range, over which the skin depth undergoes large variations. Therefore, this is a multiscale problem in three respects: (a) material properties of adjacent objects, (b) relative electrical sizes of features within the structure at a particular frequency, and (c) variations in the

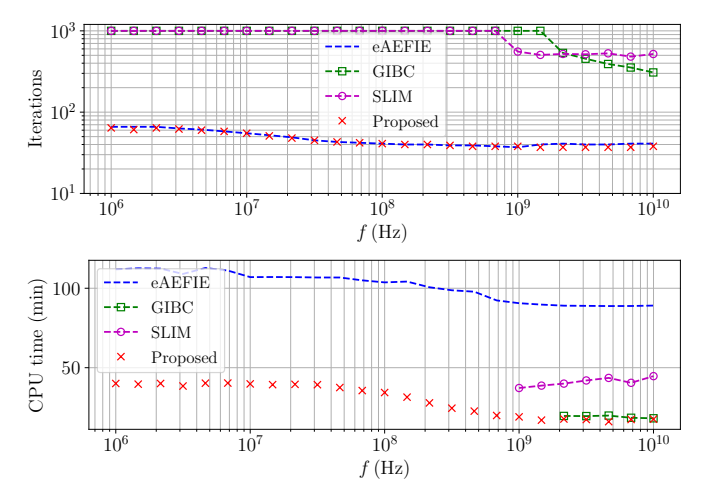


Fig. 8: Performance comparison for the inductor coil in Section IV-C. Top: GMRES iterations. Bottom: CPU time per frequency.

skin depth and the structure's overall electrical size over the considered frequency range.

The structure consists of two copper inductor coils, each of which is a $4\times$ scaled-up version of the coil described in [46], which in turn is based on [47]. The two coils are stacked back-to-back, and connected with a 2×6 array of vias. A side view of the stacked coils is shown in the bottom panel of Fig. 6. Each via has a rectangular cross section of size $3\,\mu\text{m}\times3\,\mu\text{m}$, and a height of $12\,\mu\text{m}$. The air pocket has dimensions of $210\,\mu\text{m}\times210\,\mu\text{m}\times25\,\mu\text{m}$, and is placed $10\,\mu\text{m}$ below the lower coil. The background multilayer substrate is described in the second column of Table I. The structure is meshed with $4\,758$ triangles, and is excited with two deltagap edge ports [11], as shown in Fig. 6.

Fig. 7 shows the simulated scattering (S) parameters over a broad range of frequencies, from 1 MHz to 10 GHz. The top panel shows the magnitude, while the bottom panel shows the phase. The results are compared against those from a commercial finite element solver (Ansys HFSS 2020 R2). Very good agreement is observed over the entire frequency range, and the development of skin effect is accurately captured. The top panel of Fig. 8 shows the number of GMRES iterations required for convergence, for the proposed method compared with some representative existing BEM formulations. The proposed method and the eAEFIE [22] show excellent convergence over the entire frequency range, while the GIBC [15] and SLIM [19] formulations fail to converge for frequencies below $\sim 1 \, \text{GHz}$. Even for frequencies above $\sim 1 \, \text{GHz}$, the GIBC and SLIM methods require approximately $10 \times$ more iterations. Since each port requires invoking the iterative solver, the large number of iterations required by the GIBC and SLIM approaches would become a bottleneck for structures with tens or hundreds of ports. The bottom panel of Fig. 8 shows the total CPU time taken per frequency, and shows the excellent performance of the proposed formulation in comparison to existing methods. The proposed method provides an overall 3.4× speed-up compared to the eAEFIE, by obviating

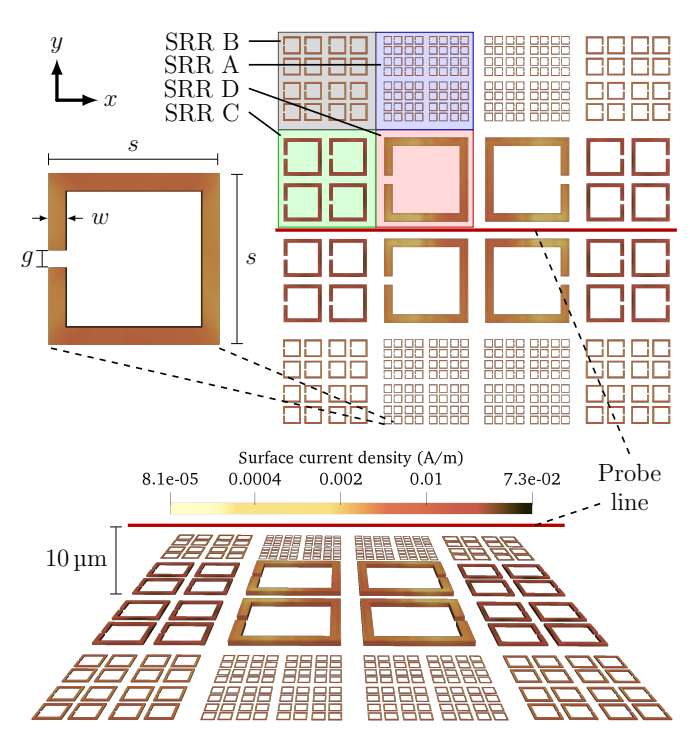


Fig. 9: Geometry and electric surface current density at 10 THz for the SRR array in Section IV-D.

TABLE II: Dimensions and electrical properties of each split ring in the SRR array in Section IV-D. Split rings are labeled based on the top panel of Fig. 9, and h denotes their height.

	s (µm)	<i>w</i> (μm)	g (μm)	h (µm)	ε_r	σ (S/m)
SRR A	2	0.2	0.2	0.1	11	0.4
SRR B	4.2	0.42	0.42	0.21	11	0.4
SRR C	9	0.9	0.9	0.45	1	5.8×10^{7}
SRR D	20	2	2	1	6	0

the need for the double-layer operator in the external problem.

D. Multiscale Split-Ring Resonator Array

Finally, we consider a multiscale array of dielectric and metallic split ring resonators (SRRs), shown in Fig. 9. SRRs are commonly used as unit cells in metasurface arrays, and can be made of dielectric or conductive materials [1], [2]. The unit cells of metasurface arrays are typically sub-wavelength in size, while the entire array may span multiple wavelengths. In addition, the arrays are typically fabricated on a substrate consisting of one or more dielectric layers. Therefore, this example is meant to be representative of the computational challenges that may be encountered in the design and analysis of multiscale electromagnetic surfaces.

As shown in Fig. 9, the structure contains four variations of unit cells. The geometry of each unit cell is identical except for a scaling factor. The top panel of Fig. 9 defines the pertinent dimensions of a single unit cell, and also shows the placement of each of the four variations of unit cells within the full array. The variations are labeled, from the smallest to the largest unit cells, as "SRR A", "SRR B", "SRR C", and "SRR D". Table II provides the dimensions for each unit cell variation. Some

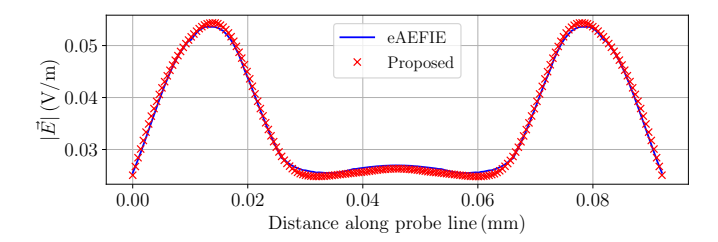


Fig. 10: Magnitude of the electric field along a probe line for the SRR array in Section IV-D, at 1 THz.

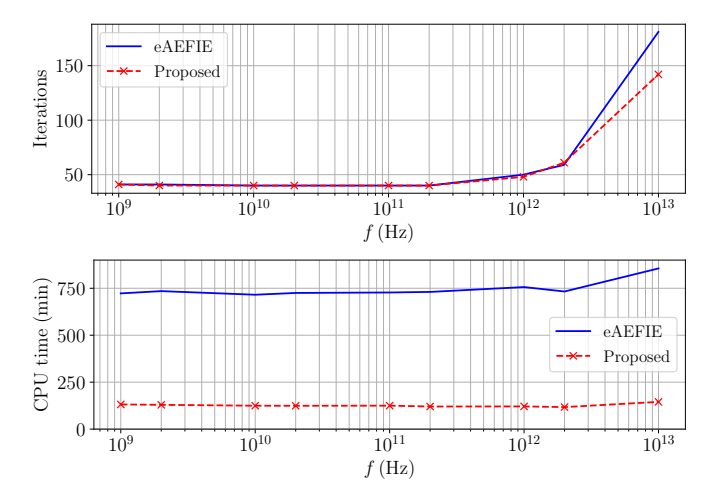


Fig. 11: Performance comparison for the SRR array in Section IV-D. Top: GMRES iterations. Bottom: CPU time per frequency.

unit cells are made of dielectric materials, while others are conductive, and the material parameters are listed in Table II. The background layered medium is described in the third column of Table I. The bottoms of all SRR unit cells are aligned at z=0, which coincides with the interface between the first (top-most) and second dielectric layers. The structure is meshed with $103\,568$ triangles, and is excited with a plane wave with the electric field oriented along the y axis, traveling in the -z direction.

Fig. 10 shows the electric field magnitude at 1 THz for the proposed method, compared to the eAEFIE, measured along the probe line shown in Fig. 9. The proposed method is in good agreement with the eAEFIE. The top panel of Fig. 11 shows that the proposed method and the eAEFIE [21] converge within a reasonable number of GMRES iterations over a broad frequency range, from 1 GHz to 10 THz. The GIBC [15] and SLIM [19] formulations did not converge within 1000 iterations for any of the frequency points considered. We were unable to simulate this structure in HFSS or Feko within the available 256 GB of memory. The bottom panel of Fig. 11 shows the total CPU time per frequency, showing the significant computational advantage of the proposed formulation compared to the eAEFIE. The proposed method yields an overall 5.9× speed-up compared to the eAEFIE formulation, reducing the total simulation time from 4.6 days to 18.9 hours. The cost of computing the double-layer potential operator in the eAEFIE is particularly disadvantageous in this case, due to the intricate and dense nature of the structure.

In summary, the numerical tests considered in this section exemplify several applications where the proposed formulation can be a compelling alternative to existing techniques, such as the GIBC [15], SLIM [19] and eAEFIE [21], [22] formulations. The proposed method yields a well-conditioned system matrix while avoiding the double-layer potential operator in the external problem, unlike the eAEFIE, leading to a significant computational advantage for structures embedded in layered media.

V. CONCLUSION

The electromagnetic modeling of complex structures with the boundary element method (BEM) requires efficient formulations, which can robustly handle multiple scales of feature size, operating frequency, and material properties of the objects. In order to obtain a well-conditioned system matrix, existing formulations require the use of expensive Buffa-Christiansen basis functions and the double-layer potential operator associated with the background medium, which is often a layered substrate. These requirements lead to a high computational cost for large problems. This article introduces a novel single-layer formulation which leads to a well-conditioned system matrix for challenging multiscale problems, while avoiding the aforementioned double-layer operator. The proposed method leverages the advantages of the Buffa-Christiansen functions while greatly alleviating the associated computational cost. Consequently, speed-ups of $3\times$ to $7 \times$ compared to existing methods are achieved for realistic structures, as demonstrated via several numerical examples.

REFERENCES

- D. Güney, T. Koschny, and C. M. Soukoulis, "Reducing ohmic losses in metamaterials by geometric tailoring," *Phys. Rev. B*, vol. 80, p. 125129, Sep. 2009.
- [2] A. Tittl, A. Leitis, M. Liu, F. Yesilkoy, D.-Y. Choi, D. N. Neshev, Y. S. Kivshar, and H. Altug, "Imaging-based molecular barcoding with pixelated dielectric metasurfaces," *Science*, vol. 360, no. 6393, pp. 1105– 1109, 2018.
- [3] T. J. Cui, W. Wiesbeck, and A. Herschlein, "Electromagnetic scattering by multiple three-dimensional scatterers buried under multilayered media. I. theory," *IEEE Trans. Geosci. Remote Sens.*, vol. 36, no. 2, pp. 526–534, Mar. 1998.
- [4] T. J. Cui and W. C. Chew, "Fast evaluation of Sommerfeld integrals for EM scattering and radiation by three-dimensional buried objects," *IEEE Trans. Geosci. Remote Sens.*, vol. 37, no. 2, pp. 887–900, Mar. 1999.
- [5] K. Yang and A. E. Yilmaz, "A three-dimensional adaptive integral method for scattering from structures embedded in layered media," *IEEE Trans. Geosci. Remote Sens.*, vol. 50, no. 4, pp. 1130–1139, Apr. 2012.
- [6] J.-W. Lin, C. Chen, and Y.-T. Cheng, "A robust high-Q micromachined RF inductor for RFIC applications," *IEEE Trans. Electron Devices*, vol. 52, no. 7, pp. 1489–1496, Jun. 2005.
- [7] P. J. Bell, N. D. Hoivik, R. A. Saravanan, N. Ehsan, V. M. Bright, and Z. Popovic, "Flip-chip-assembled air-suspended inductors," *IEEE Trans. Adv. Packag.*, vol. 30, no. 1, pp. 148–154, Feb. 2007.
- [8] Z. Zhang and X. Liao, "Micromachined GaAs MMIC-based spiral inductors with metal shores and patterned ground shields," *IEEE Sensors* J., vol. 12, no. 6, pp. 1853–1860, Dec. 2012.
- [9] D. Colton and R. Kress, Integral Equation Methods in Scattering Theory. Hoboken, NJ, USA: Wiley, 1983.
- [10] W. Chew, M. Tong, and B. Hu, Integral Equation Methods for Electromagnetic and Elastic Waves. San Rafael, CA, USA: Morgan & Claypool, 2008.

- [11] W. C. Gibson, The Method of Moments in Electromagnetics. Boca Raton, FL, USA: CRC press, 2014.
- [12] A. Poggio and E. Miller, "Integral equation solutions of three-dimensional scattering problems," in *Computer Techniques for Electromagnetics*, ser. International Series of Monographs in Electrical Engineering. Pergamon, 1973, pp. 159 264.
- [13] Y. Chang and R. Harrington, "A surface formulation for characteristic modes of material bodies," *IEEE Trans. Antennas Propag.*, vol. 25, no. 6, pp. 789–795, Nov. 1977.
- [14] T. Wu and L. L. Tsai, "Scattering from arbitrarily-shaped lossy dielectric bodies of revolution," *Radio Sci.*, vol. 12, no. 5, pp. 709–718, Sep. 1977.
- [15] Z. G. Qian, W. C. Chew, and R. Suaya, "Generalized impedance boundary condition for conductor modeling in surface integral equation," *IEEE Trans. Microw. Theory Tech.*, vol. 55, no. 11, pp. 2354–2364, Nov. 2007.
- [16] Z.-G. Qian, M. S. Tong, and W. C. Chew, "Conductive medium modeling with an augmented GIBC formulation," *Prog. Electromagn. Res.*, vol. 99, pp. 261–272, 2009.
- [17] W. Chai and D. Jiao, "Direct matrix solution of linear complexity for surface integral-equation-based impedance extraction of complicated 3-D structures," *Proc. IEEE*, vol. 101, no. 2, pp. 372–388, Jun. 2013.
- [18] K. A. Michalski and J. R. Mosig, "Multilayered media Green's functions in integral equation formulations," *IEEE Trans. Antennas Propag.*, vol. 45, no. 3, pp. 508–519, Mar. 1997.
- [19] S. Sharma and P. Triverio, "SLIM: A well-conditioned single-source boundary element method for modeling lossy conductors in layered media," *IEEE Antennas Wireless Propag. Lett.*, vol. 19, no. 12, pp. 2072– 2076, Sep. 2020.
- [20] S. Rao, D. Wilton, and A. Glisson, "Electromagnetic scattering by surfaces of arbitrary shape," *IEEE Trans. Antennas Propag.*, vol. 30, no. 3, pp. 409–418, May 1982.
- [21] T. Xia, H. Gan, M. Wei, W. C. Chew, H. Braunisch, Z. Qian, K. Aygün, and A. Aydiner, "An enhanced augmented electric-field integral equation formulation for dielectric objects," *IEEE Trans. Antennas Propag.*, vol. 64, no. 6, pp. 2339–2347, Jun. 2016.
- [22] ——, "An integral equation modeling of lossy conductors with the enhanced augmented electric field integral equation," *IEEE Trans. An*tennas Propag., vol. 65, no. 8, pp. 4181–4190, Aug. 2017.
- [23] Z.-G. Qian and W. C. Chew, "An augmented electric field integral equation for high-speed interconnect analysis," *Microw. Opt. Technol. Lett.*, vol. 50, no. 10, pp. 2658–2662, 2008.
- [24] —, "Fast full-wave surface integral equation solver for multiscale structure modeling," *IEEE Trans. Antennas Propag.*, vol. 57, no. 11, pp. 3594–3601, Nov. 2009.
- [25] A. Buffa and S. H. Christiansen, "A dual finite element complex on the barycentric refinement," *Math. Computation*, vol. 76, pp. 1743–1769, 2007.
- [26] D. De Zutter and L. Knockaert, "Skin effect modeling based on a differential surface admittance operator," *IEEE Trans. Microw. Theory Tech.*, vol. 53, no. 8, pp. 2526 – 2538, Aug. 2005.
- [27] U. R. Patel, S. V. Hum, and P. Triverio, "A novel single-source surface integral method to compute scattering from dielectric objects," *IEEE Antennas Wireless Propag. Lett.*, vol. 16, pp. 1715–1718, Feb. 2017.
- [28] U. R. Patel, P. Triverio, and S. V. Hum, "A single-source surface integral equation formulation for composite dielectric objects," in *IEEE Int. Symp. Antennas Propag. USNC-URSI Radio Sci. Meeting*, 2017, pp. 1453–1454.
- [29] S. Sharma and P. Triverio, "A single-source surface impedance formulation for modeling arbitrary penetrable media," in *IEEE Int. Symp. Antennas Propag. USNC-URSI Radio Sci. Meeting*, Montreal, QC, Jul. 2020
- [30] ——, "A well-conditioned differential surface admittance formulation for modeling penetrable media," in *IEEE Int. Symp. Antennas Propag.* USNC-URSI Radio Sci. Meeting, Atlanta, GA, Jul. 2019.
- [31] Z. G. Qian and W. C. Chew, "A quantitative study on the low frequency breakdown of EFIE," *Microw. Opt. Technol. Lett.*, vol. 50, no. 5, pp. 1159–1162, 2008.
- [32] F. P. Andriulli, K. Cools, H. Bagci, F. Olyslager, A. Buffa, S. Christiansen, and E. Michielssen, "A multiplicative calderon preconditioner for the electric field integral equation," *IEEE Trans. Antennas Propag.*, vol. 56, no. 8, pp. 2398–2412, Aug. 2008.
- [33] M. Gossye, M. Huynen, D. Vande Ginste, D. De Zutter, and H. Rogier, "A Calderón preconditioner for high dielectric contrast media," *IEEE Trans. Antennas Propag.*, vol. 66, no. 2, pp. 808–818, Feb. 2018.
- [34] S. Sharma, P. Triverio, "Accelerated boundary element modeling of lossy conductors in layered media with a single-source surface impedance

- operator," in *IEEE Conf. Electr. Perform. Electron. Packag. Syst.*, San Jose, CA, Oct. 2020.
- [35] S. Sharma, U. R. Patel, S. V. Hum, and P. Triverio, "A complete surface integral method for broadband modeling of 3D interconnects in stratified media," arXiv e-prints, p. arXiv: 1810.04030, Oct. 2018.
- [36] W. C. Chew, Waves and Fields in Inhomogeneous Media. Hoboken, NJ, USA: Wiley, 1999.
- [37] R. F. Harrington, Time-Harmonic Electromagnetic Fields. Hoboken, NJ, USA: Wiley, 1961.
- [38] E. Bleszynski, M. Bleszynski, and T. Jaroszewicz, "AIM: Adaptive integral method for solving large-scale electromagnetic scattering and radiation problems," *Radio Sci.*, vol. 31, no. 5, pp. 1225–1251, Sep. 1996
- [39] S. Sharma and P. Triverio, "An accelerated surface integral equation method for the electromagnetic modeling of dielectric and lossy objects of arbitrary conductivity," *IEEE Trans. Antennas Propag.*, Mar. 2021 (early access).
- [40] O. Wiedenmann and T. F. Eibert, "The effect of near-zone preconditioning on electromagnetic integral equations of first and second kind," Advances Radio Sci., vol. 11, pp. 61–65, 2013.
- [41] Y. Saad and M. Schultz, "GMRES: A generalized minimal residual algorithm for solving nonsymmetric linear systems," SIAM J. Scientific Statistical Comput., vol. 7, no. 3, pp. 856–869, 1986.
- [42] S. Balay, S. Abhyankar M. F. Adams, J. Brown, P. Brune, K. Buschelman, L. Dalcin, V. Eijkhout, W. D. Gropp, D. Kaushik, M. G. Knepley, D. A. May, L. C. McInnes R. T. Mills, T. Munson, K. Rupp, P. Sanan B. F. Smith, S. Zampini, H. Zhang. *PETSc Web Page*. (2019). Accessed: Nov. 01, 2019. Available: http://www.mcs.anl.gov/petsc.
- [43] F. Crameri, "Scientific colour maps," Feb. 2021. [Online]. Available: https://doi.org/10.5281/zenodo.4491293
- [44] E. Simsek, Q. H. Liu, and B. Wei, "Singularity subtraction for evaluation of Green's functions for multilayer media," *IEEE Trans. Microw. Theory Tech.*, vol. 54, no. 1, pp. 216–225, Jan. 2006.
- [45] K. A. Michalski and J. R. Mosig, "Efficient computation of Sommerfeld integral tails - methods and algorithms," *J. Electromagn. Waves Appl.*, vol. 30, no. 3, pp. 281–317, 2016.
- [46] U. R. Patel, S. Sharma, S. Yang, S. V. Hum, and P. Triverio, "Full-wave electromagnetic characterization of 3D interconnects using a surface integral formulation," in *IEEE Conf. Electr. Perform. Electron. Packag.* Syst., San Jose, CA, Oct. 2017.
- [47] T. Moselhy, FastMaxwell User's Manual, MIT. [Online]. Available: http://web.mit.edu/ tmoselhy/www/FastMaxwell